ADVANCING EARTH AND SPACE SCIENCES

JGR Atmospheres

RESEARCH ARTICLE
10.1029/2026JD047813

Structure and Dynamics of the Boreal Late-Summer East Asian Monsoon Interannual Variability

Ying Guo[1,2], Kaiming Hu[3], and Gang Huang[1,2]

[1]State Key Laboratory of Earth System Numerical Modeling and Application, Institute of Atmospheric Physics, Chinese Academy of Sciences, Beijing, China, [2]University of Chinese Academy of Sciences, Beijing, China, [3]College of Resource Environment and Tourism, Capital Normal University, Beijing, China

Key Points:

- Dominant mode of the late-summer East Asian monsoon features a deep anticyclonic/cyclonic circulation tilting northwestward with height
- This mode is maintained by extracting kinetic and potential energy from the background flow
- The anomalies of late-summer East Asian precipitation are primarily induced by temperature advection associated with this mode

Supporting Information:

Supporting Information may be found in the online version of this article.

Correspondence to:

K. Hu and G. Huang,
hkm@mail.iap.ac.cn;
hg@mail.iap.ac.cn

Citation:

Guo, Y., Hu, K., & Huang, G. (2026). Structure and dynamics of the boreal late-summer East Asian monsoon interannual variability. *Journal of Geophysical Research: Atmospheres*, *131*, e2026JD047813. https://doi.org/10.1029/2026JD047813

Received 17 JUN 2026
Accepted 25 JUL 2026

Author Contributions:

Conceptualization: Kaiming Hu
Data curation: Ying Guo
Formal analysis: Ying Guo
Methodology: Ying Guo, Kaiming Hu
Project administration: Kaiming Hu
Supervision: Kaiming Hu, Gang Huang
Visualization: Ying Guo
Writing – original draft: Ying Guo
Writing – review & editing: Ying Guo, Kaiming Hu, Gang Huang

Abstract Pronounced interannual variability of the late-summer (July–August) East Asian summer monsoon exerts strong influences on flood and drought events across East Asia, yet the underlying processes governing this variability remain poorly understood. Using reanalysis data, we identify the dominant mode of circulation variability that captures the dominant interannual variability of the late-summer East Asian monsoon system. The mode features a troposphere-deep anticyclonic/cyclonic circulation, tilting northwestward with height, within the westerly jet exit region. This mode is dynamically maintained by extracting kinetic and potential energy from the background flow. The jet exit region enables the mode to gain eddy kinetic energy from the background field. Meanwhile, its northwestward-tilting vertical structure facilitates the extraction of available potential energy from the meridional temperature gradient over East Asia. Vorticity budget analysis reveals that this northwestward-tilting vertical structure arises from the vertical shear of climatological northerlies on the eastern flank of the summer South Asian High. In turn, the mode drives vertical motion anomalies via temperature advection, regulating precipitation anomalies of the late-summer East Asian monsoon.

Plain Language Summary Late-summer rainfall over East Asia varies greatly from year to year and can lead to severe floods or droughts, affecting millions of people. However, the physical processes behind these changes are still not fully understood. In this study, we identify a large-scale atmospheric pattern that plays a key role in controlling these variations. This pattern extends throughout the troposphere and is closely linked to the East Asian upper-level jet and climatological temperature fields. We show that interactions between this pattern and the jet help maintain its structure and influence the vertical motion associated with precipitation. Overall, our results highlight the importance of interactions between the jet and background temperature in regulating late-summer East Asian monsoon variability and hydrological extremes.

1. Introduction

The East Asian summer monsoon serves as a crucial component of the global monsoon system and exerts a profound influence on the hydroclimate of densely populated regions across East Asia (Ding, 2004; Ding & Chan, 2005; Lau, 1992). The monsoon is characterized primarily by the northward migration of the primary rainband. For example, during boreal early summer (May–June), the rainband gradually migrates northward from southern China and reaches northern China and the Korean Peninsula in boreal late-summer period (July–August) (Figure S1 in Supporting Information S1; Feng & Hu, 2004; Han et al., 2015; Wang et al., 2013). Interannual variability of the boreal late-summer monsoon can therefore exert a substantial influence on hydroclimate conditions across East Asia, frequently leading to severe floods and droughts with considerable socioeconomic impacts (Seo et al., 2012; Wang et al., 2001).

Compared with boreal early summer, the large-scale circulation over East Asia undergoes substantial reorganization during the boreal late-summer period. Prominent features include the northward displacement of the western North Pacific subtropical high, low-level monsoonal southwesterlies, and the upper-tropospheric westerly jet (S. Li et al., 2024; Lu, 2004; Wang et al., 2009). Among these circulation systems, the westerly jet plays a particularly important role in regulating regional climate variability (Ding, 1992; G. Huang & Liu, 2011). For instance, southeast-northwest displacements of the jet can substantially influence precipitation over North China and India, maybe leading to out-of-phase precipitation anomalies between the two regions (Du et al., 2016; Wei et al., 2017). In addition, both the Pacific-Japan (PJ) pattern and the Silk Road Pattern (SRP) are closely associated with the westerly jet and can extract energy from the background flow to sustain their development (Kosaka & Nakamura, 2006; Kosaka et al., 2009). These patterns represent important modes of interannual climate variability over the Asian monsoon region and exert substantial influences on regional circulation and precipitation (Enomoto et al., 2003; R. Y. Lu et al., 2002; Nitta, 1987). The PJ pattern is associated with circulation anomalies over the western North Pacific and the SRP is characterized by a circum-Eurasian teleconnection wave train extending across the Eurasian continent (R. Y. Lu et al., 2002; Nitta, 1987). However, during the boreal late-summer period, it remains unclear whether the East Asian westerly jet region hosts a distinct circulation mode associated with East Asian summer monsoon interannual variability. If such a mode exists, what dynamical processes govern its formation and maintenance, and how does it influence East Asian precipitation?

The remainder of this paper is organized as follows. Section 2 describes the diagnostic methods employed in this study, and Section 3 introduces the data sets used. Section 4 presents the main results. In this section, we first identify the leading mode of interannual variability in the East Asian westerly jet region and characterize its associated circulation and precipitation anomalies. And then we investigate the processes responsible for the formation and maintenance of this mode from the perspectives of Rossby wave source and energetics. Finally, we explore how this circulation mode modulates interannual precipitation variability over East Asia through large-scale atmospheric circulation anomalies. Section 5 summarizes the main findings, discusses the limitations of the present study, and outlines directions for future research.

2. Data

All data sets used in this study cover the period 1979–2025. Boreal late-summer precipitation is defined as the total precipitation accumulated during July-August, whereas other atmospheric variables, including horizontal wind, vertical velocity, and air temperature, are represented by their July–August means.

Precipitation data are obtained from the Global Precipitation Climatology Project (GPCP) monthly precipitation data set, with a horizontal resolution of $2.5° \times 2.5°$ (Adler et al., 2003). Atmospheric circulation fields are derived from the NCEP/DOE Reanalysis II data set (Kanamitsu et al., 2002), provided by the NOAA Physical Sciences Laboratory (PSL, Boulder, Colorado, USA; https://psl.noaa.gov). The data set has a horizontal resolution of $2.5° \times 2.5°$ and includes daily horizontal wind, vertical velocity, geopotential height, and air temperature fields. Monthly mean horizontal wind and air temperature fields from the fifth-generation European Centre for Medium-Range Weather Forecasts (ECMWF) reanalysis (ERA5) are additionally used as an independent data set to support several key findings of this study. Statistical significance was assessed using a two-tailed Student's t-test.

3. Methods

3.1. Multivariate Empirical Orthogonal Function (MV-EOF) Analysis

During the boreal late-summer period (July–August, JA), East Asia is located within the exit region of the upper-tropospheric westerly jet and exhibits pronounced variability in horizontal winds, as indicated by the large standard deviations of the 200-hPa wind field during 1979–2025 (Figure 1a). To identify the dominant modes of interannual variability in the upper-tropospheric circulation during boreal late-summer period, July–August mean 200-hPa horizontal winds are calculated for each year during 1979–2025, and the MV-EOF analysis was performed on the zonal and meridional wind components (u, v) over the domain (20°–60°N, 90°–150°E) (T. Lu et al., 2024; Wang, 1992). Note that in this study, "interannual variability" refers to the year-to-year variations of the mean circulation field during boreal late-summer period. Within the MV-EOF framework, it is represented by the interannual fluctuations of the principal-component amplitudes associated with the leading circulation modes, rather than by changes in the spatial patterns of the modes themselves. MV-EOF analysis is essentially an eigenvalue decomposition of a covariance matrix constructed from multiple variables and the calculations are given as follows.

First, the climatological mean for the period 1979–2025 was removed from the 200-hPa zonal and meridional wind fields to obtain the anomaly fields (u' and v').

$$X = [u', v'] \tag{1}$$

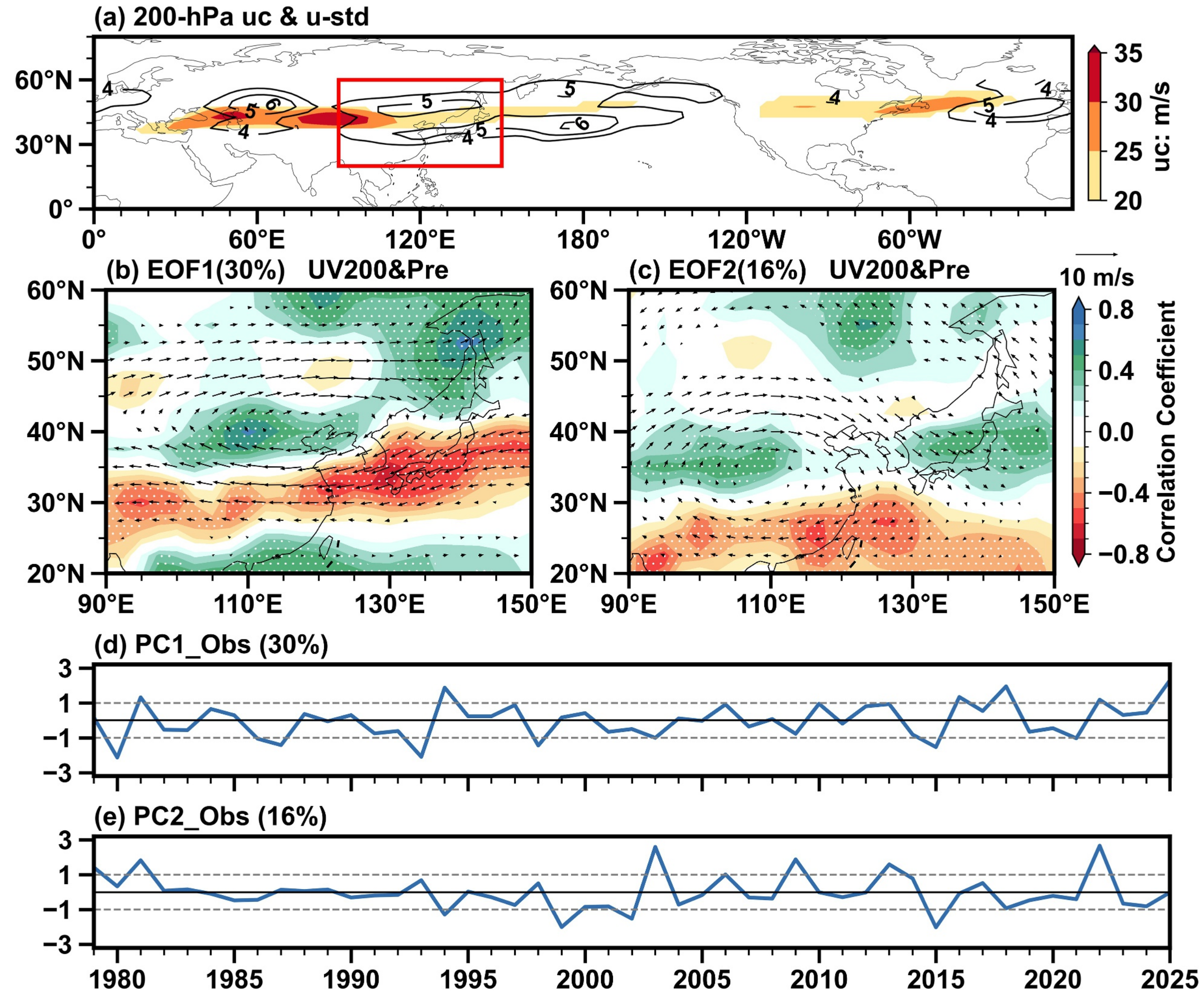

Figure 1. Leading modes of upper-tropospheric circulation variability over East Asia during the late-summer period (July–August). (a) Climatological 200-hPa zonal wind during the late-summer period and its interannual standard deviation for 1979–2025 (shading: wind speed; contours: standard deviation). The red box indicates the analysis domain (20°–60°N, 90°–150°E). The first mode (b) and the second mode (c) of 200-hPa horizontal wind anomalies. Vectors denote wind anomalies significant at the 95% confidence level. Shading shows the correlation between the standardized principal components (PC1_Obs in b; PC2_Obs in c) and late-summer precipitation. White stippling indicates regions where correlations are significant at the 95% confidence level.

$$C = \frac{1}{N-1} X^T X \tag{2}$$

$$Ce_i = \lambda_i e_i \; (i = 1, 2, 3 \ldots) \tag{3}$$

where X denotes the combined anomaly matrix composed of the zonal and meridional wind anomalies, C is the covariance matrix, λ_i is the eigenvalue, e_i is the corresponding eigenvector, and N is the sample size, 47. The leading EOF modes were obtained from the eigenvectors associated with the largest eigenvalues. The normalized principal component time series associated with the first and second MV-EOF modes are hereafter denoted as PC1_Obs and PC2_Obs, respectively.

Following North et al. (1982), neighboring modes were considered statistically distinct when the separation between their eigenvalues exceeded the estimated sampling error.

$$N_{\mathrm{eff}} \approx N \frac{1-\rho_i}{1+\rho_i} \tag{4}$$

$$\delta\lambda_i \approx \lambda_i \sqrt{\frac{2}{N_{\mathrm{eff}}}} \tag{5}$$

where $\delta\lambda_i$ denotes the sampling error of the i-th eigenvalue. N_{eff} represents effective sample size and ρ_i is the lag-1 autocorrelation coefficient estimated from the corresponding principal component (e.g., PC1_Obs, PC2_Obs). Following North et al. (1982), two neighboring modes are considered statistically distinct when

$$\lambda_i - \lambda_{i+1} > \delta\lambda_i \tag{6}$$

3.2. Analysis of Vertical Motions

To clarify the anomalous vertical motion, we analyze the related dynamics through the linearized omega equation (Trenberth, 1978; Yin et al., 2023). This equation consists of three terms, the vorticity-advection term ($\omega'_{\mathrm{vortadv}}$), the temperature-advection term (ω'_{tadv}) and the diabatic-heating feedback term ($\omega'_{\mathrm{diabatic}}$).

$$\omega' = \omega'_{\mathrm{vortadv}} + \omega'_{\mathrm{tadv}} + \omega'_{\mathrm{diabatic}} \tag{7}$$

$\omega'_{\mathrm{vortadv}}$ represents anomalous vertical motion induced by anomalous vorticity advection. The specific calculation is given as follows:

$$\omega'_{\mathrm{vortadv}} = \left(\nabla^2 + \frac{f^2}{\sigma}\frac{\partial^2}{\partial p^2}\right)^{-1} \frac{f}{\sigma}\frac{\partial}{\partial p}\left(\overline{u}\frac{\partial \xi'}{\partial x} + \overline{v}\frac{\partial \xi'}{\partial y} + u'\frac{\partial \overline{\xi}}{\partial x} + v'\frac{\partial \overline{\xi}}{\partial y} + v'\frac{\partial f}{\partial y}\right) \tag{8}$$

Here, u', v' and ξ' respectively represent the anomalous horizontal winds and relative vorticity anomalies regressed onto PC1_Obs, while $\overline{u}$, $\overline{v}$ and $\overline{\xi}$ denote those of climatology (1979–2025). Calculations for other variables marked with overbars and primes are performed analogously.

ω'_{tadv} measures the vertical-velocity anomaly induced by anomalous temperature advection and is estimated based on the following formula:

$$\omega'_{\mathrm{tadv}} = \left(\nabla^2 + \frac{f^2}{\sigma}\frac{\partial^2}{\partial p^2}\right)^{-1} \frac{R\sigma}{p}\nabla^2\left(\overline{u}\frac{\partial T'}{\partial x} + \overline{v}\frac{\partial T'}{\partial y} + u'\frac{\partial \overline{T}}{\partial x} + v'\frac{\partial \overline{T}}{\partial y}\right) \tag{9}$$

Notably, the vertical velocities inverted from $\overline{u}\frac{\partial T'}{\partial x}$, $\overline{v}\frac{\partial T'}{\partial y}$, $u'\frac{\partial \overline{T}}{\partial x}$, $v'\frac{\partial \overline{T}}{\partial y}$ are referred to as ω'_{B1}, ω'_{B2}, ω'_{B3}, ω'_{B4}, respectively.

$\omega'_{\mathrm{diabatic}}$ quantifies the contribution of diabatic heating to vertical-velocity anomalies. Diabatic heating includes latent heat release, sensible heat transport, radiative heating and so on. Precipitation is accompanied by latent heat release, while latent heat release can in turn enhance atmospheric ascent through diabatic heating and thereby promote precipitation. Owing to this close coupling, the diabatic-heating term represents an important feedback component in the interaction between vertical motion and precipitation. Following Yanai et al. (1973), $\omega'_{\mathrm{diabatic}}$ can be calculated from the following two equations

$$\omega'_{\mathrm{diabatic}} = -\left(\nabla^2 + \frac{f^2}{\sigma}\frac{\partial^2}{\partial p^2}\right)^{-1} \frac{R\sigma}{C_p \cdot p}\nabla^2(q') \tag{10}$$

$$q = C_p\left[\frac{\partial T}{\partial t} + \mathrm{u}\frac{\partial T}{\partial x} + v\frac{\partial T}{\partial y} + \omega\frac{\partial \theta}{\partial p}\left(\frac{p}{p0}\right)^{\frac{R}{C_p}}\right] \tag{11}$$

10.1029/2026JD047813

It should be noted that Equation 11 is evaluated using daily data. The daily results are first averaged over July-August, and the resulting July-August mean values are then substituted into Equation 10 for the calculation of $\omega'_{\text{diabatic}}$. Here, $\sigma = \left(\frac{R\overline{T}}{C_p p}\right) - \left(\frac{\partial \overline{T}}{\partial p}\right)$, denotes the climatological static stability, which is consistently positive from 1,000 hPa to 200 hPa in JA (Figure S6 in Supporting Information S1). f, R, and C_p are the Coriolis parameter, gas constant (287 J K^{-1} kg^{-1}), and specific heat at constant pressure (1,004 J K^{-1} kg^{-1}), respectively. $\theta = T\left(\frac{P_o}{p}\right)^{\frac{R}{C_p}}$, denotes the potential temperature and ω is the vertical velocity in pressure coordinates (unit: Pa/s).

3.3. Analysis About Rossby Wave Source

Using the linearized vorticity equation, we diagnose the vorticity budget of circulation anomalies associated with the leading mode of interannual precipitation variability in East Asia (Hu et al., 2018; Kosaka & Nakamura, 2006).

$$S' \underbrace{-\overline{u}_{\psi}\frac{\partial \xi'}{\partial x}}_{\text{ZA}} \underbrace{-\overline{v}_{\psi}\frac{\partial \xi'}{\partial y}}_{\text{MA}} \underbrace{\underbrace{-u'_{\psi}\frac{\partial \overline{\xi}}{\partial x}}_{\beta_1} \underbrace{-v'_{\psi}\frac{\partial \left(f+\overline{\xi}\right)}{\partial y}}_{\beta_2}}_{\beta} - \text{Residual} = 0 \tag{12}$$

Here, ξ denotes relative vorticity. u_{ψ} and v_{ψ} are the zonal and meridional components of the rotational wind, whereas u_{χ} and v_{χ} in the following equation are the corresponding components of the divergent wind. The horizontal wind field was decomposed into rotational (nondivergent) and divergent (irrotational) components using the Helmholtz decomposition implemented through the spherical harmonic routines of the NCAR Command Language (NCL).

The term ZA and MA represent the advections of anomalous vorticity by climatological zonal and meridional winds, respectively. The β term denotes the horizontal advection of the mean absolute vorticity by anomalous horizontal winds and can be decomposed into β_1 and β_2. Specifically, β_1 denotes the zonal advection of $\overline{\xi}$ by the anomalous rotational wind u'_{ψ}, whereas β_2 denotes the meridional advection of $\left(f + \overline{\xi}\right)$ by v'_{ψ}. Furthermore, the β_2 term can be further decomposed into β_{21} $(-v'_{\psi}\frac{\partial f}{\partial y})$ and β_{22} $(-v'_{\psi}\frac{\partial \overline{\xi}}{\partial y})$. Vertical advection, tilting, and nonlinear effects are included in the Residual term. S' represents the linearized barotropic Rossby wave source, the computations are shown below (Sardeshmukh & Hoskins, 1988).

$$S' = \underbrace{-u'_{\chi}\frac{\partial \overline{\xi}}{\partial x} - v'_{\chi}\frac{\partial \left(f+\overline{\xi}\right)}{\partial y}}_{S'_{11}} \underbrace{-\left(f+\overline{\xi}\right)\left(\frac{\partial u'_{\chi}}{\partial x} + \frac{\partial v'_{\chi}}{\partial y}\right)}_{S'_{12}} \underbrace{-\overline{u_{\chi}}\frac{\partial \xi'}{\partial x} - \overline{v_{\chi}}\frac{\partial \xi'}{\partial y}}_{S'_{21}} \underbrace{-\xi'\left(\frac{\partial \overline{u_{\chi}}}{\partial x} + \frac{\partial \overline{v_{\chi}}}{\partial y}\right)}_{S'_{22}} \tag{13}$$

S'_{11} denotes the advection of climatological absolute vorticity by the anomalous divergent wind; S'_{12} denotes the stretching term of the anomalous divergent wind, weighted by the background absolute vorticity $\left(f + \overline{\xi}\right)$. S'_{21} denotes the advection of anomalous relative vorticity ξ' by the climatological divergent wind, and S'_{22} denotes the stretching of ξ' associated with the divergence of the climatological divergent wind. Positive values of ZA, MA, β, and S' indicate contributions that favor the development or intensification of cyclonic circulation.

3.4. Energetic Diagnostics

We apply energy diagnostics to diagnose the sources and maintenance of interannual precipitation variability in East Asia. The local barotropic conversion from the mean flow to perturbations (CK), which measures the transfer from mean kinetic energy to eddy kinetic energy (EKE), is estimated based on the following formula (Hu et al., 2018; Kosaka & Nakamura, 2006; T. Lu et al., 2025; Simmons et al., 1983).

$$\mathrm{CK} = \underbrace{\frac{\left(v'^2 - u'^2\right)}{2}\left(\frac{\partial \overline{u}}{\partial x} - \frac{\partial \overline{v}}{\partial y}\right)}_{\mathrm{CK}_x} \underbrace{-u'v'\left(\frac{\partial \overline{u}}{\partial y} + \frac{\partial \overline{v}}{\partial x}\right)}_{\mathrm{CK}_y} \tag{14}$$

CK_x describes the energy conversion from the background confluent flow to perturbations, whereas CK_y denotes the energy conversion from the mean horizontal wind shear to perturbations. Note that the confluence in this study denotes the directional convergence of the zonal or meridional wind components, different from total horizontal wind convergence. Positive CK indicates the energy conversion from the background mean flow to anomalous atmospheric patterns, contributing to their development.

To measure the efficiency of CK at 200 hPa in the maintenance of the leading mode, we evaluate the time scale:

$$\tau_{\mathrm{CK}} = \frac{\langle \mathrm{EKE} \rangle}{\langle \mathrm{CK} \rangle} \tag{15}$$

The brackets represent the area mean over the domain [20°–60°N, 90°–150°E] and the τ_{CK} denotes how long it takes for the local EKE associated with anomalous patterns ($\mathrm{EKE} = \frac{(u'^2 + v'^2)}{2}$) to be fully replenished through CK.

The local baroclinic energy conversion rate (PC), from mean available potential energy (MAPE) to eddy available potential energy (EAPE) is diagnosed based on the following equation.

$$\mathrm{CP} = \frac{1}{g}\int_{200}^{1000} \left(\underbrace{\frac{f}{\sigma} u'T' \frac{\partial \overline{v}}{\partial p}}_{\mathrm{CP}_x} \underbrace{- \frac{f}{\sigma} v'T' \frac{\partial \overline{u}}{\partial p}}_{\mathrm{CP}_y} \right) \mathrm{dp} \tag{16}$$

Here, p denotes pressure, and the square brackets indicate a vertical integral from 1,000 hPa to 200 hPa. Since the static stability parameter σ is positive, the sign of CP is primarily determined by the eddy heat flux ($u'T'$ and $v'T'$) and background state ($\frac{\partial \overline{v}}{\partial p}$ and $\frac{\partial \overline{u}}{\partial p}$). Positive CP indicates a conversion from mean available potential energy (MAPE) to eddy available potential energy (EAPE), thereby promoting the growth of perturbations. CP_x and CP_y denote the zonal and meridional contributions to CP, respectively. Similar to barotropic energy conversion, we estimate the time scale of effective CP for maintaining the leading mode.

$$\mathrm{EAPE}_v = \frac{1}{g}\int_{200}^{1000} \frac{\mathrm{RT}'^2}{2\sigma p} \mathrm{dp} \tag{17}$$

$$\tau_{\mathrm{CP}} = \frac{\langle \mathrm{EAPE}_v \rangle}{\langle \mathrm{CP} \rangle} \tag{18}$$

EAPE_v stands for the vertically integrated EAPE associated with anomalous patterns, and τ_{CP} measures the efficiency of CP in supplying local EAPE to perturbations.

Note that the energy conversion terms are quadratic in the perturbations (e.g., u'^2, v'^2, $u'v'$, $u'T'$, and $v'T'$) and therefore remain unchanged during the negative phase of the MV-EOF mode. Accordingly, the diagnostics for the positive phase also apply to the negative phase, implying that the energy conversion processes are phase-independent. It should be noted that the energy diagnostic equations used in this study are based on a linearized framework and therefore do not consider nonlinear interactions among eddies at different scales.

4. Results

4.1. The Dominant Mode of Late-Summer Upper-Tropospheric Circulation Over East Asia

During boreal late-summer period, the climatological 200-hPa zonal wind places East Asia within the subtropical jet-exit region, where interannual variability of the upper-level flow is maximized (Figure 1a). The leading modes of upper-tropospheric circulation variability over East Asia are identified using multivariate EOF analysis of the 200-hPa horizontal wind over [20°–60°N, 90°–150°E]. The first two modes are well separated according to North's test (Figures 1b and 1c). The first mode, accounting for approximately 30% of the total variance, represents the primary pattern of upper-tropospheric circulation variability and is characterized by an anomalous anticyclone centered near 40°N within the jet-exit region.

The positive phase of the dominant mode is associated with a pronounced tripolar precipitation anomaly pattern over East Asia. Specifically, when a large-scale anomalous anticyclone occupies the upper troposphere over East Asia, precipitation increases over northern China, while a band of negative precipitation anomalies extends from the Yangtze River Basin to Japan. Positive precipitation anomalies are also observed over southern China and the Philippine Sea (Figure 1b). In addition, PC1_Obs successfully captures several major hydroclimatic events, including the floods over northern China in 1994 (T. Li & Gao, 1995), 2012 (Yu, 2012), and 2025 (X. Li et al., 2025), as well as the severe drought over the Yangtze River Basin in 2022 (Ma et al., 2022) (Figure 1d). In contrast, the negative phase of the mode is characterized by an anomalous cyclone in the upper troposphere, accompanied by below-normal precipitation over northern China, positive precipitation anomalies extending from the Yangtze River Basin to Japan, and negative precipitation anomalies over southern China and the Philippine Sea.

The dominant mode of upper-tropospheric circulation variability during boreal late-summer period is insensitive to the choice of analysis domain. To assess its robustness, we perform an additional MV-EOF analysis of the 200-hPa horizontal wind over a larger domain (15°–65°N, 85°–155°E). The leading mode explains approximately 26% of the total variance. The circulation and precipitation anomaly patterns associated with its positive phase are highly similar to those shown in Figure 1b, confirming the robustness of the identified mode (Figure S2 in Supporting Information S1).

Furthermore, an independent EOF analysis of boreal late-summer precipitation reveals that the positive phase of the dominant precipitation mode exhibits a tripolar anomaly structure that closely resembles the precipitation pattern shown in Figure 1b (Figure S3 in Supporting Information S1). The principal component associated with the dominant precipitation EOF mode exhibits a correlation coefficient of 0.61 with PC1_Obs. This result indicates that the dominant upper-tropospheric circulation mode identified in this study is significantly and closely linked to the dominant mode of boreal late-summer precipitation variability over East Asia.

Figure 2 illustrates the anomalous circulation structure associated with PC1_Obs at different tropospheric levels. A coherent large-scale anticyclonic circulation extends throughout the troposphere, appearing at 925, 500, and 200 hPa. Notably, the circulation centers exhibit a pronounced northwestward tilt with height, shifting from the region between the Korean Peninsula and Japan at low levels to northern East Asia near 40°N in the upper troposphere. Between 35°N and 50°N, the positive phase of the mode is associated with positive temperature anomalies and anomalous ascending motion over East Asia (Figure 2d). In contrast, anomalous descending motion prevails between 25°N and 30°N. The strongest vertical-motion anomalies within the 25°–50°N latitudinal band are concentrated in the mid-troposphere, with maximum amplitudes occurring near 500 hPa. South of 25°N, a deep layer of anomalous ascent extends throughout the troposphere, from near 1,000 hPa to the tropopause.

4.2. Dynamical Formation and Maintenance of the Dominant Circulation Mode

To understand the dynamical formation and maintenance of the northwestward-tilting circulation structure identified above, we examine the vorticity balance associated with the dominant mode using the linearized quasi-stationary Rossby wave source equation (Equation 12; see "Methods"). The following analysis focuses on the positive phase of the dominant mode, as the analysis for the negative phase is analogous. Figure 3f shows the 200-hPa relative vorticity anomalies corresponding to PC1_Obs. Negative vorticity anomalies dominate northern China and the Korean Peninsula, while positive anomalies extend from the Yangtze River Basin to the Northwestern Pacific, consistent with the anomalous circulation pattern of the dominant mode shown in Figure 1b.

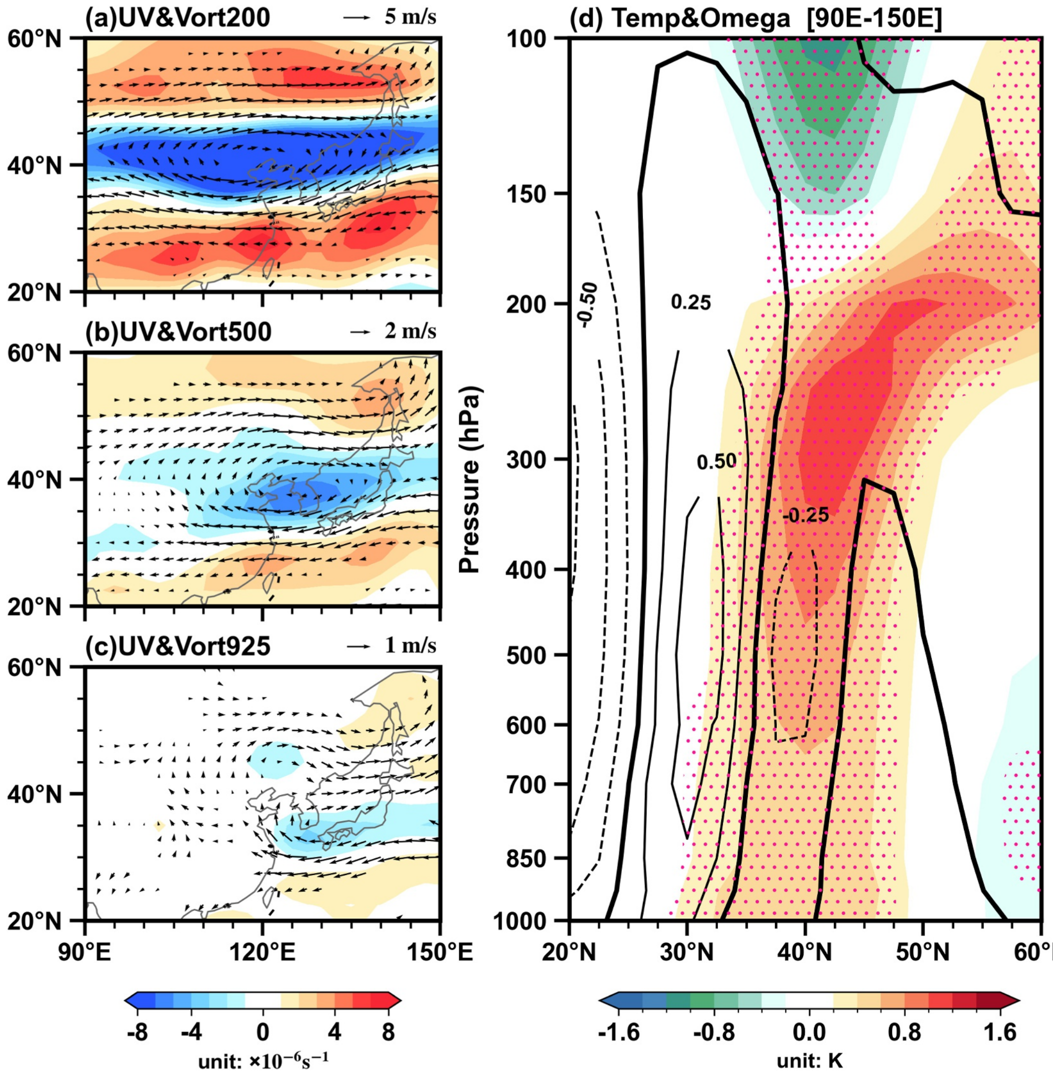

Figure 2. Vertical structure of anomalous circulation associated with PC1_Obs during the late-summer period over East Asia (20°–60°N, 90°–150°E). (a) Anomalous horizontal winds at 200 hPa. Vectors are shown where anomalies are significant at the 99% confidence level. The shading denotes the vorticity anomalies corresponding to PC1_Obs, with units of $\times 10^{-6}\ \mathrm{s}^{-1}$. Panels (b and c) show the conditions at 500 hPa and 925 hPa, respectively. (d) Longitude-averaged vertical velocity (contours, unit: $\times 10^{-2}$ Pa s^{-1}) and temperature (shading, unit: K) anomalies, averaged over 90°–150°E. Pink dots indicate regions significant at the 99% confidence level, and thick black contours denote zero values.

Diagnosis of the individual terms in Equation 12 indicates that the Residual term is relatively small and spatially scattered compared with the meridional advection (MA_{200}), β-effect (β_{200}), zonal advection (ZA_{200}), and Rossby wave source terms (Figure 3). This suggests that the upper-tropospheric circulation anomalies are primarily governed by these dynamical components, providing a basis for understanding the generation of the leading circulation mode.

The diagnosed vorticity balance demonstrates that the anomalous circulation associated with the leading mode behaves as a quasi-stationary Rossby wave over East Asia. The zonal advection (ZA_{200}) and planetary vorticity advection (β_{200}) display opposite signs and largely offset each other (Figures 3b and 3d), indicating a near balance typical of quasi-stationary wave dynamics. The β_{200} term is primarily controlled by the advection of climatological absolute vorticity by anomalous meridional rotational winds, the β_2 term (Figure S4 in Supporting Information S1).

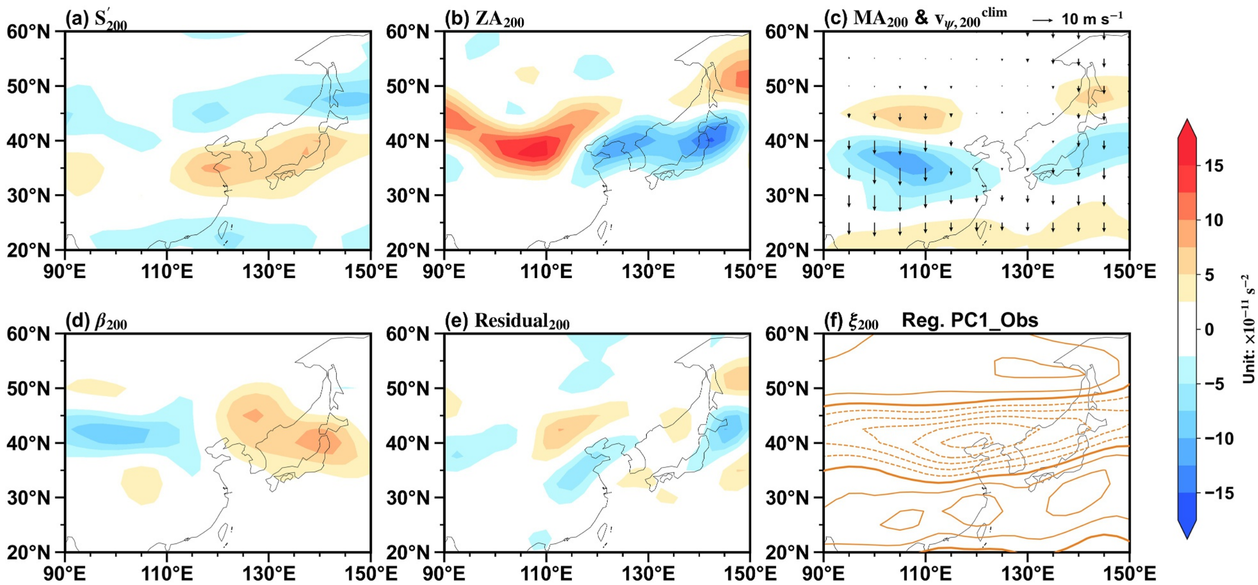

Figure 3. Rossby wave source diagnostics associated with the anomalous anticyclone at 200 hPa regressed onto PC1_Obs. Climatological and anomalous rotational winds are denoted by $(\overline{u_\psi}, \overline{v_\psi})$ and (u'_ψ, v'_ψ) respectively and climatological and anomalous relative vorticity by $\overline{\xi}$ and ξ' respectively. (a) Rossby wave source term (S'_{200}). (b) Zonal advection term (ZA$_{200}$; $-\overline{u_\psi}\frac{\partial \xi'}{\partial x}$). (c) Meridional advection term (shading, $-\overline{v_\psi}\frac{\partial \xi'}{\partial y}$; MA$_{200}$) with climatological meridional rotational wind vectors ($\overline{v_\psi}$). (d) Planetary vorticity advection term (β_{200}; $-u'_\psi\frac{\partial \overline{\xi}}{\partial x} - v'_\psi\frac{\partial (f+\overline{\xi})}{\partial y}$). (e) The residual term. (f) Relative vorticity anomalies regressed onto PC1_Obs (contours; 2.5×10^{-6} s^{-1}). Thin orange solid (dashed) contours denote positive (negative) values, and thick contours indicate zero.

The Rossby wave source term (S'_{200}) shows a pronounced meridional tripolar structure over East Asia, with positive anomalies between 30° and 40°N and negative anomalies to the north and south (Figure 3a). Diagnostic analysis reveals that this structure mainly results from the stretching term of the anomalous divergent wind (S'_{12}, Equation 13) and together with advection of anomalous vorticity by the background divergent flow, S'_{22} (Figures 4b and 4c). Over the region extending from the Yangtze River Basin to the Northwestern Pacific, anomalous upper-tropospheric convergence associated with decreased precipitation may imply reduced latent heat release, probably contributing to the formation of positive Rossby wave forcing between 30°N and 40°N. Under the climatological late-summer circulation dominated by the South Asian High, northerly mean flow brings anomalous vorticity southward, balancing the Rossby wave forcing and thereby sustaining the quasi-stationary circulation anomalies. Together, these results indicate that the large-scale circulation anomalies associated with the leading mode are jointly maintained by quasi-stationary Rossby wave forcing within the jet-exit region and the climatological northerly flow under the South Asian High.

To examine the dynamical balance of circulation anomalies in the lower troposphere, the vorticity budget at 925 hPa is analyzed. At this level, the vorticity balance is dominated by the wave-source and residual terms, whereas other dynamical contributions are comparatively weak over East Asia (Figure 5). The results show that the Rossby wave source term (S'_{925}) is largely balanced by the Residual term, whereas the contributions from the meridional advection, zonal advection, and β-effect terms are relatively weak over East Asia (Figure 5). In addition, the wave-source term is primarily associated with the stretching of the anomalous divergent wind (Figure S5 in Supporting Information S1).

We further examine the maintenance of the leading circulation mode from an energetics perspective. To quantify the kinetic energy exchange between the mean flow and circulation anomalies, the barotropic kinetic energy conversion (CK) for 200 hPa is analyzed (Du et al., 2016; R. H. Huang & Liu, 2011; Lu, 2004). Positive CK indicates transfer of kinetic energy from the background jet to circulation anomalies. At 200 hPa, the spatial distribution of CK over East Asia exhibits four distinct centers, with positive centers located west of 120°E and negative centers located to the east (Figure 6c). The zonally elongated eddy structure ($u'^2 > v'^2$) favors extraction of kinetic energy from the confluent background flow, particularly south of the jet axis where horizontal shear is

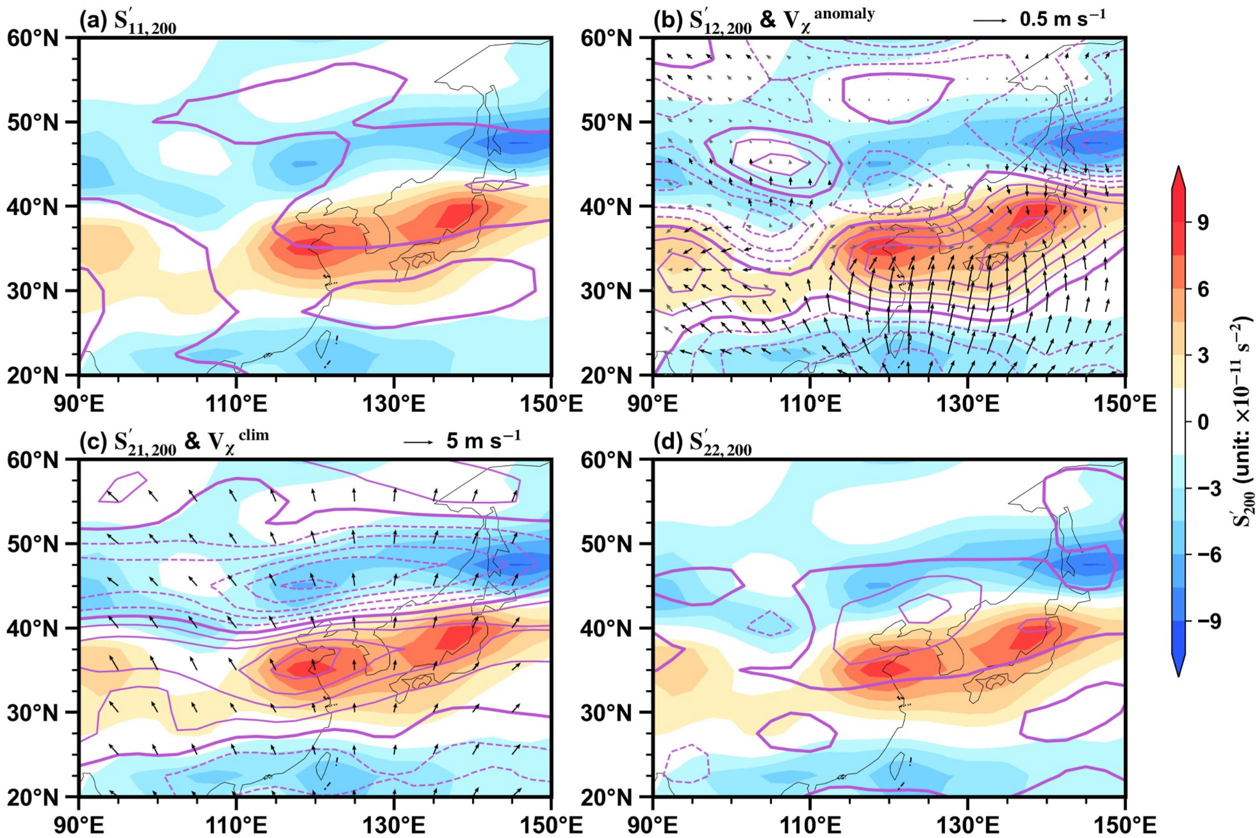

Figure 4. Decomposition of the Rossby wave source term at 200 hPa (S'_{200}). Anomalous and climatological divergent winds are denoted by (u'_χ, v'_χ) and ($\overline{u_\chi}$, $\overline{v_\chi}$) respectively. Shading shows S'_{200} in all four panels and purple contours denote individual contributions to the wave source term at intervals of ±1, ±2, ±3, and $\pm 4 \times 10^{-11}$ s^{-1}; thick contours indicate zero values. (a) Contribution from advection of climatological absolute vorticity by anomalous divergent winds (S'_{11}). (b) Contribution from divergence of anomalous divergent winds acting on climatological absolute vorticity (S'_{12}). (c) Contribution from advection of anomalous vorticity by climatological divergent winds (S'_{21}). (d) Contribution from divergence of climatological divergent winds acting on anomalous vorticity (S'_{22}).

strongest (Figure 6a). This interaction enables perturbations to efficiently draw energy from the climatological jet, thereby reinforcing the upper-tropospheric circulation anomalies.

We further calculate the area-weighted mean values of CK, CK_x and CK_y over the study domain, and they are 6.16×10^{-6}, 6.69×10^{-6} and -0.53×10^{-6} m^2/s^3 respectively. On a regional-mean basis, the perturbations gain barotropic energy mainly from CK_x over East Asia. To quantify the efficiency of CK in maintaining the 200-hPa circulation anomalies, we evaluate the time scale τ_{CK} (see "Methods," Equation 15). It's shown that the EKE is 3.28 m^2/s^2 and τ_{CK} is 6.17 days, suggesting barotropic conversion effectively sustains the anomalous circulation against dissipation.

In addition to kinetic energy supply, baroclinic energy conversion (CP) also provides an important source of EAPE. Vertically integrated CP exhibits a tripole structure aligned with the jet axis, primarily contributed by the meridional component (CP_y). The positive CP north of 35–40°N indicates efficient conversion of MAPE into perturbation energy, supporting the persistence and vertical structure of the leading circulation mode. The area-weighted averages of CP, CP_x, and CP_y over the domain [20°–60°N, 90°–150°E] are 1.97×10^{-2}, -1.13×10^{-2}, 3.09×10^{-2} W/m^2, respectively. The area-weighted mean EAPE is 3.01×10^4 Jm^{-2}, and the corresponding τ_{cp} is 17.71 days (see "Methods", Equations 17 and 18).

The energetics characteristics of the identified mode are particularly noteworthy. The energy-renewal timescale associated with CK is approximately one-third of that associated with CP, and both timescales are shorter than 30 days. This indicates that the mode can efficiently extract energy from the background flow and effectively compensate for low-level dissipation, thereby sustaining its development (Watanabe, 2005).

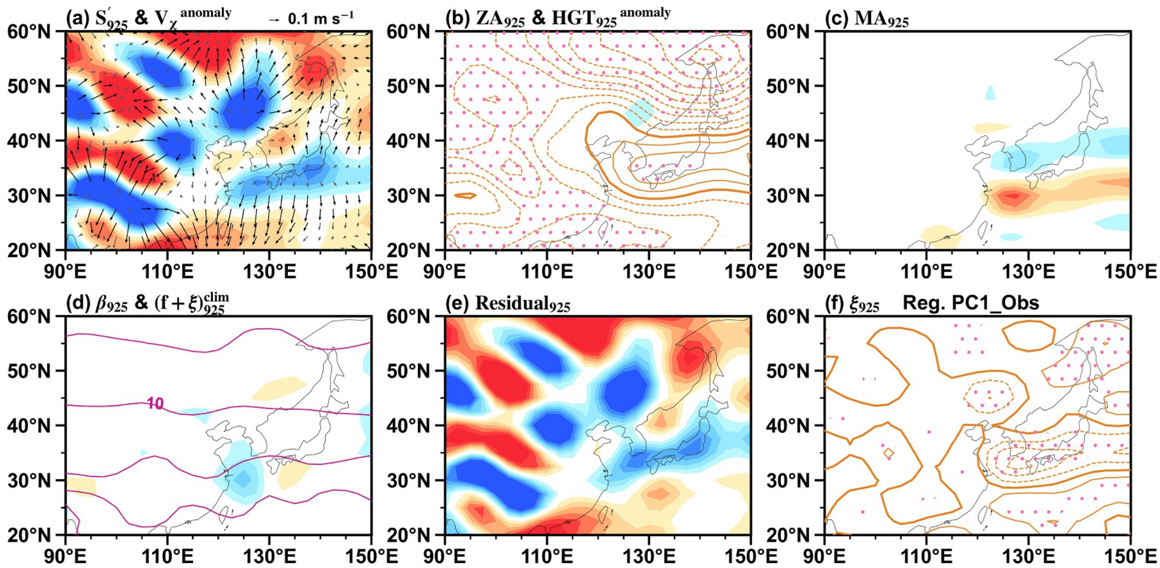

Figure 5. Rossby wave source diagnostics associated with the leading-mode anomalous anticyclone at 925 hPa. Shading in panels (a–e) corresponds to the same dynamical terms as in Figure 3. (a) Anomalous divergent wind (vectors). (b) Anomalous geopotential height (contours; interval: 1 geopotential meter (gpm)), with thick orange contours indicating zero values. (d) Climatological absolute vorticity (contours; interval $2 \times 10^{-6}\ s^{-1}$). (f) Relative vorticity anomalies (contours; interval $1 \times 10^{-6}\ s^{-1}$). Pink stippling in panels (b and f) indicates regions significant at the 90% confidence level.

Compared with the Silk Road Pattern (SRP), the present mode exhibits substantially different energetics characteristics. For the SRP, the CP energy-renewal timescale is approximately one-third of the CK timescale, and the spatial location of the mode is strongly constrained by the distribution of CK (Kosaka et al., 2009). In contrast, the latitudinal position of the mode identified in this study appears to be anchored by the climatological northerlies on the eastern flank of the South Asian High in the upper troposphere. These results suggest that the two modes are maintained through different dynamical processes.

The zonal-mean structure further shows that positive CP extends through much of the troposphere north of 35°N, indicating deep baroclinic energy conversion consistent with the vertically tilted circulation structure identified in Figure 2, thereby contributing to the persistence of the vertically coherent circulation anomalies.

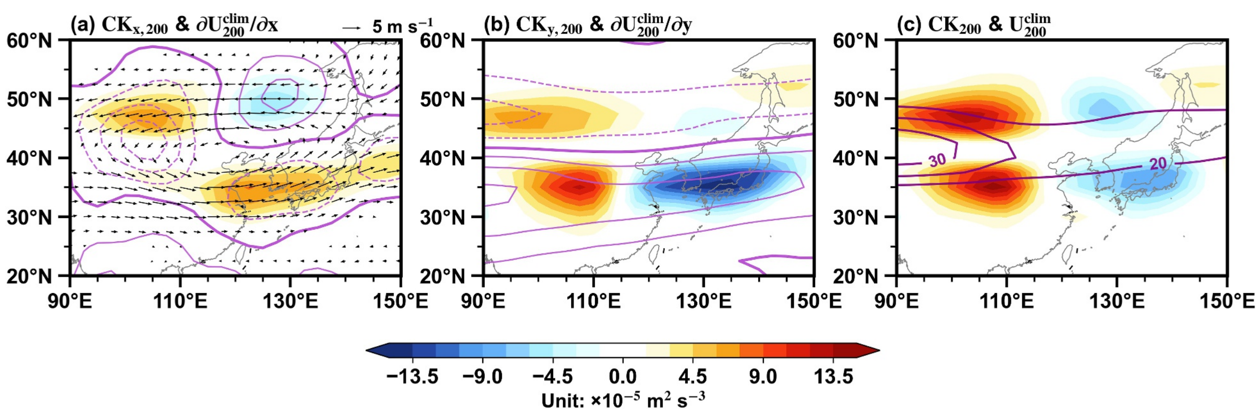

Figure 6. Barotropic kinetic energy conversion (CK) at 200 hPa associated with the leading circulation mode over East Asia (20°–60°N, 90°–150°E). Thin solid (dashed) contours denote positive (negative) values. (a) Zonal component of barotropic energy conversion (CK_x; shading). Vectors show horizontal wind anomalies regressed onto PC1_Obs (significant at the 95% confidence level). Thin contours denote the zonal gradient of climatological zonal wind (interval $2 \times 10^{-6}\ s^{-1}$). (b) Meridional component of barotropic energy conversion (CK_y; shading). Thin contours denote the meridional gradient of climatological zonal wind (interval $1 \times 10^{-5}\ s^{-1}$). (c) Total barotropic energy conversion ($CK = CK_x + CK_y$; shading). Purple contours show climatological zonal wind at 20, 25, and 30 m s^{-1}. Thick purple contours in panels (a, b) indicate zero values.

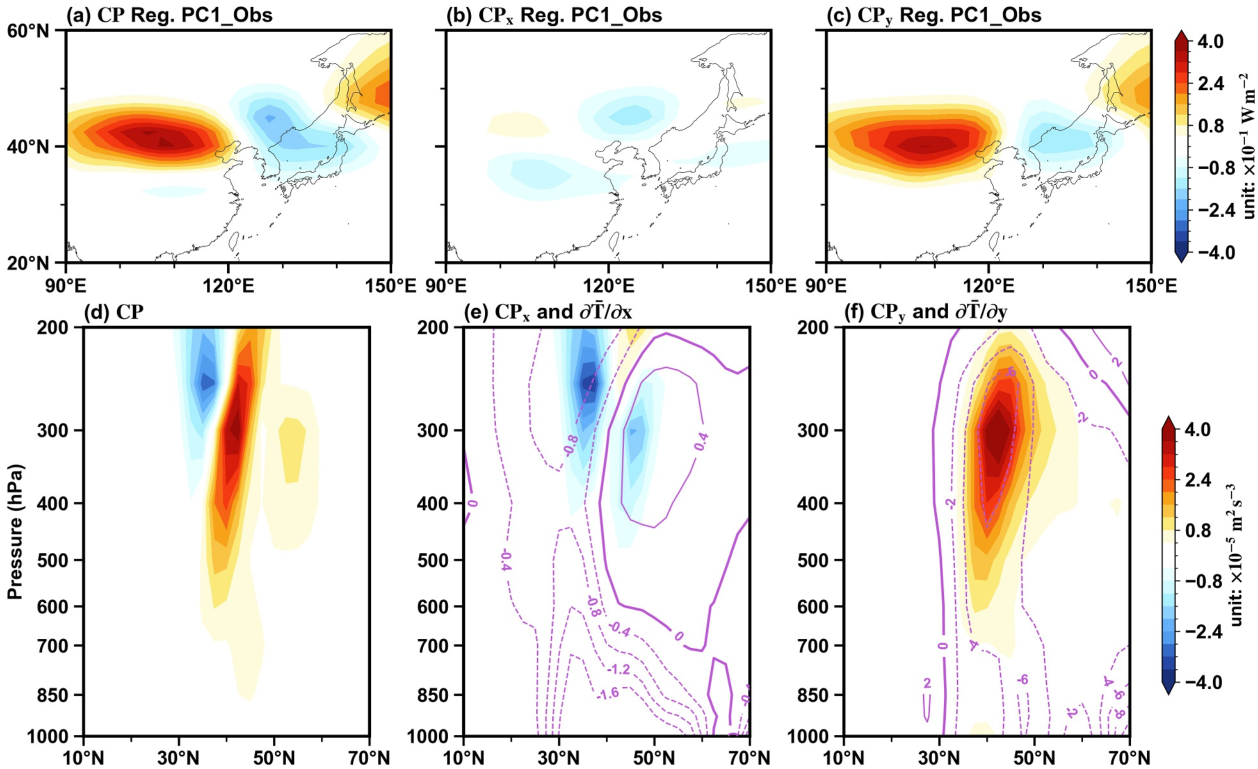

Figure 7. Baroclinic energy conversion associated with the leading circulation mode. Contours denote climatological 200-hPa zonal wind speed at 20, 25, and 30 m s^{-1}. (a) Vertically integrated baroclinic energy conversion (CP) from 1,000 to 200 hPa ($\times10^{-1}$ W m^{-2}). (b, c) Vertically integrated zonal (CP_x) and meridional (CP_y) components of CP, respectively (same units as in a). (d) Zonal-mean CP averaged over 90°–150°E ($\times10^{-5}$ m^2 s^{-3}). (e, f) Zonal-mean CP_x and CP_y, respectively (same units as in panel (d)).

Based on the thermal-wind relation, the vertical structure of CP is closely linked to perturbation winds and temperature acting on the climatological horizontal temperature gradients (Holton & Hakim, 2013). With positive static stability throughout 1,000–200 hPa over East Asia (Figure S6 in Supporting Information S1), Equation 16 indicates that CP_x and CP_y are governed by $-u'T'\ \frac{\partial \overline{T}}{\partial x}$ and $-v'T'\frac{\partial \overline{T}}{\partial y}$, respectively; that is, baroclinic conversion is controlled by perturbation heat fluxes relative to the background temperature gradients.

The vertical structures of temperature anomalies and anomalous winds averaged over 90°–150°E show distinct zonal and meridional heat-transport characteristics (Figure S7 in Supporting Information S1). In the upper troposphere, $u'T'$ is predominantly negative over 30°–40°N but becomes positive over 40°–50°N, implying a reversal in the zonal eddy heat transport relative to the background zonal temperature gradient (Figure 7e). Consistent with Equation 16, this contributes to negative CP_x in the upper troposphere, indicating conversion from EAPE to MAPE in association with zonal heat transport. In contrast, $v'T'$ is positive through much of the troposphere between 30° and 50°N (Figure S7 in Supporting Information S1), corresponding to a net northward eddy heat transport that acts against the negative climatological meridional temperature gradient ($\frac{\partial \overline{T}}{\partial y} < 0$; Figure 7f). This yields positive CP_y, indicating efficient conversion from MAPE to EAPE via meridional heat transport.

Taken together, the CP's structure indicates that baroclinic energy conversion is primarily associated with the meridional component. Meanwhile, the disturbance development and maintenance appear to be more closely related to CK, consistent with the vertically tilted anticyclonic structure of the leading mode in the jet-exit region. This characteristic differs from that of the PJ pattern and SRP pattern (Kosaka & Nakamura, 2006; Kosaka et al., 2009).

10.1029/2026JD047813

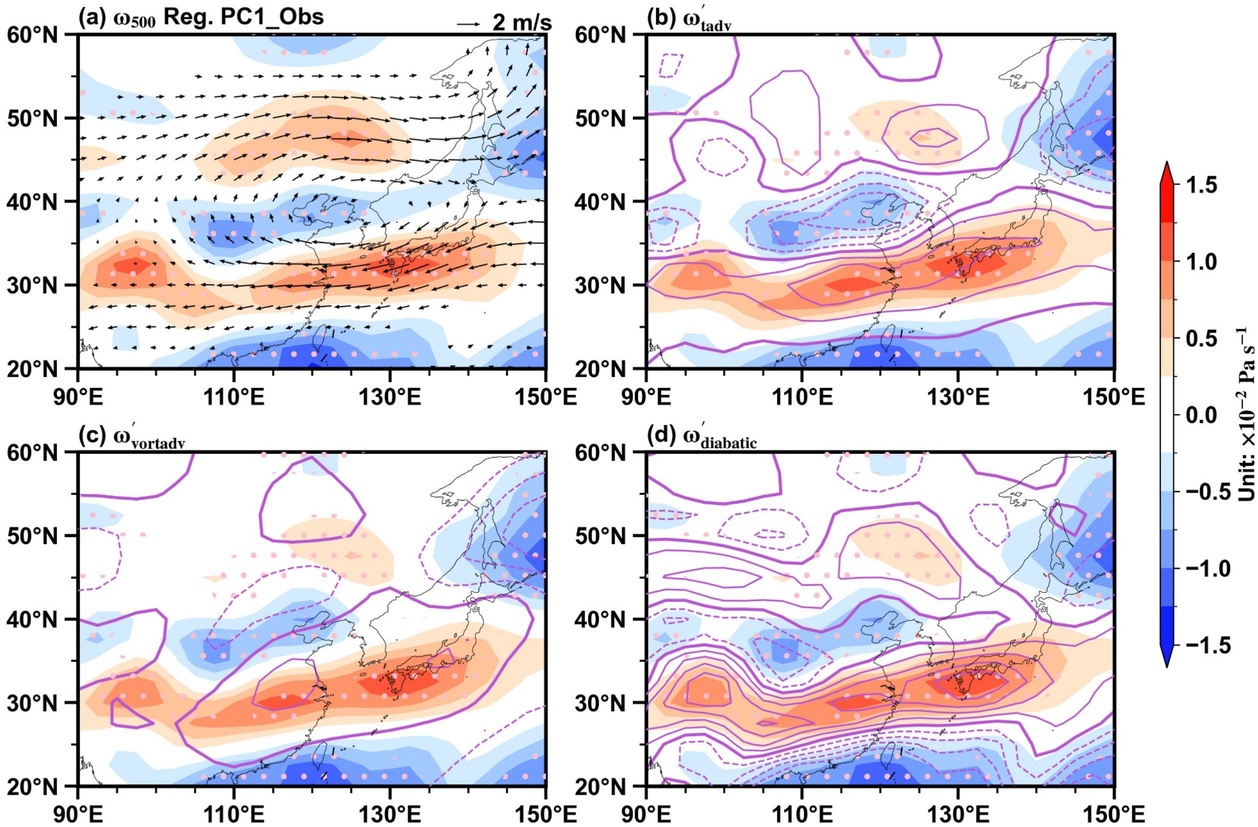

Figure 8. Vertical motion associated with the leading circulation mode at 500 hPa and its dynamical decomposition based on the quasi-geostrophic omega equation. (a) Horizontal wind anomalies at 500 hPa regressed onto PC1_Obs; vectors are shown only where regression coefficients are significant at the 95% confidence level. Shading in (a–d) denotes anomalous vertical velocity at 500 hPa regressed onto PC1_Obs. Contours represent diagnosed vertical motion forced by temperature advection (b), vorticity advection (c), and diabatic heating (d). Thin purple solid (dashed) contours indicate positive (negative) values at ±0.15, ±0.30, ±0.45, and ±0.60 Pa s^{-1}; thick contours denote zero.

4.3. Circulation-Induced Modulation of Late-Summer Precipitation Over East Asia

Having established the formation and energetic maintenance of the dominant circulation mode, we next investigate how it influences boreal late-summer precipitation over East Asia through anomalous atmospheric circulation. To address this question, we employ the quasi-geostrophic omega equation (Equations 7–11, see "Methods") and compare the reconstructed anomalous vertical velocity with the vertical-motion anomalies shown in Figure 2d. In addition, the quasi-geostrophic omega equation allows the contributions of temperature advection and vorticity advection to anomalous vertical motion to be quantitatively separated. Because diabatic heating and precipitation are coupled through complex two-way interactions, this study does not attempt to diagnose the direct contribution of diabatic heating to vertical motion. Instead, we only discuss its potential feedback effects.

Figure 8a shows the anomalous mid-tropospheric vertical velocity associated with the positive phase of the leading mode. Pronounced anomalous ascent occurs over northern China, whereas anomalous subsidence extends from the Yangtze River Basin to southern Japan. The spatial distribution of the vertical-motion anomalies closely resembles the precipitation anomaly pattern shown in Figure 1b, indicating a dynamically consistent relationship among the circulation, vertical-motion, and precipitation anomalies associated with the leading mode. However, because the quasi-geostrophic diagnosis is based on a simplified linear dynamical framework and does not fully account for ageostrophic motions and nonlinear interactions, some discrepancies between the diagnosed and observed fields are expected.

Compared with the contributions from temperature advection and diabatic-heating feedbacks, the vertical-motion anomalies associated with vorticity advection are relatively small (ω'_{tadv}; Figure 8b). Positive temperature-

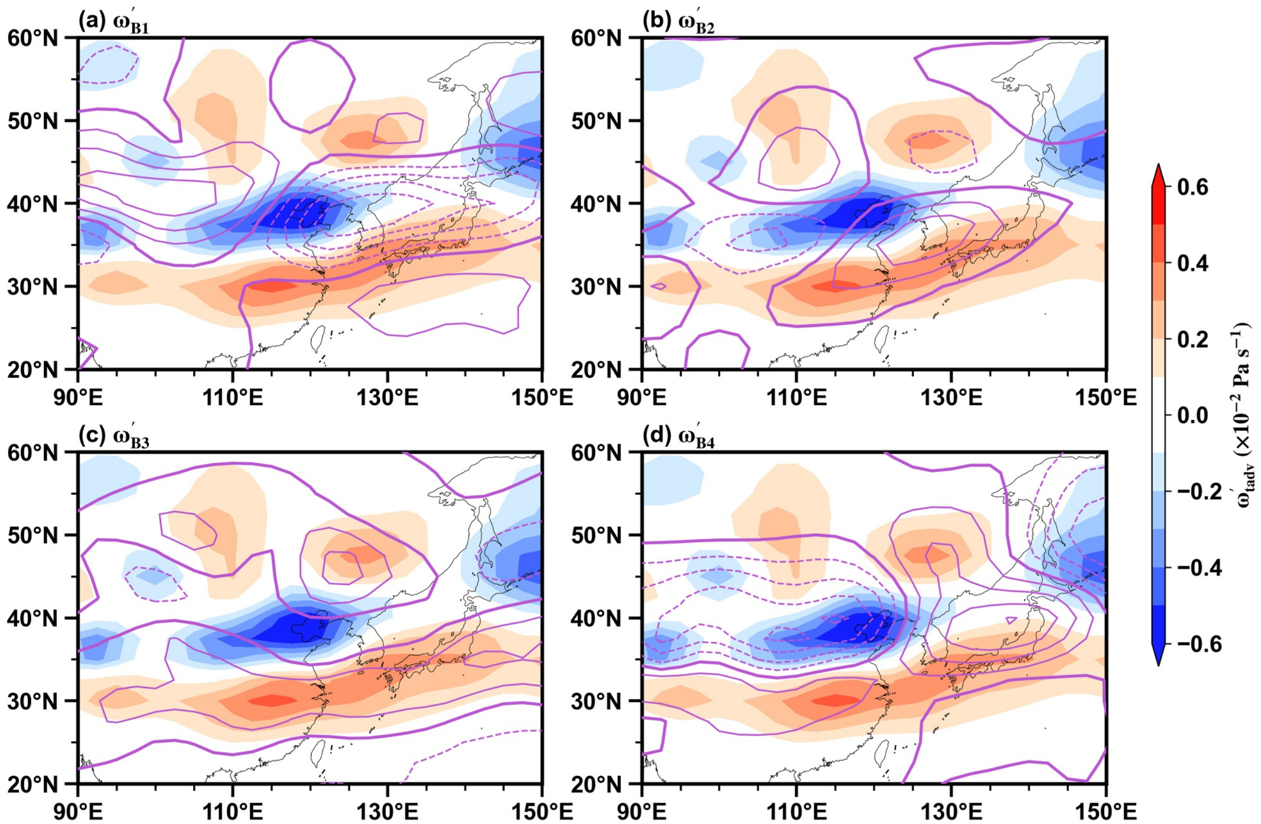

Figure 9. Decomposition of vertical motion forced by temperature advection at 500 hPa based on the quasi-geostrophic omega equation. Shading denotes anomalous vertical velocity induced by temperature advection (ω'_{tadv}; same as Figure 8b). Thin purple solid (dashed) contours indicate positive (negative) values at ±0.1, ±0.2, ±0.3, ±0.4, ±0.5 and ±0.6 Pa s^{-1}, and thick contours denote zero. Contours in panels (a–d) show vertical motion diagnosed from the linearized temperature-advection components associated with $-\bar{u}\frac{\partial T'}{\partial x}$, $-\bar{v}\frac{\partial T'}{\partial y}$, $-u'\frac{\partial \bar{T}}{\partial x}$, and $-v'\frac{\partial \bar{T}}{\partial y}$, respectively.

advection forcing generates anomalous ascent over northern China, while negative temperature-advection forcing produces anomalous subsidence from the Yangtze River Basin to southern Japan ($\omega'_{\mathrm{diabatic}}$; Figure 8d).

To further clarify the dynamical origin of temperature advection, the linearized temperature-advection term is decomposed into four components representing advection of temperature anomalies by the mean flow and advection of the climatological temperature by anomalous winds (Figure 9). Among these components, the dominant contribution arises from $-v'\frac{\partial \bar{T}}{\partial y}$ (ω'_{B4}, Equation 9, see Methods) over the primary East Asian rainband region, indicating that anomalous meridional winds acting on the climatological meridional temperature gradient primarily control the vertical-motion response. A secondary contribution originates from $-\bar{u}\frac{\partial T'}{\partial x}$ (ω'_{B1}; Figure 9a), associated with advection of temperature anomalies by the background westerlies.

The dominance of ω'_{B4} reflects the configuration of the climatological thermal structure and anomalous circulation over East Asia. At 500 hPa, a pronounced meridional temperature gradient exists north of 30°N, with warmer air located to the south (Figure S8 in Supporting Information S1). The anomalous southerlies associated with the leading mode transport warm air northward, producing strong warm advection and dynamically induced ascent. Similarly, background westerlies advect positive temperature anomalies eastward, reinforcing warm advection downstream of the temperature-anomaly center (Figure S9 in Supporting Information S1). These processes collectively link anomalous circulation to thermally forced vertical motion and associated precipitation anomalies. Together, these results demonstrate that the dominant mode regulates precipitation primarily through anomalous temperature advection.

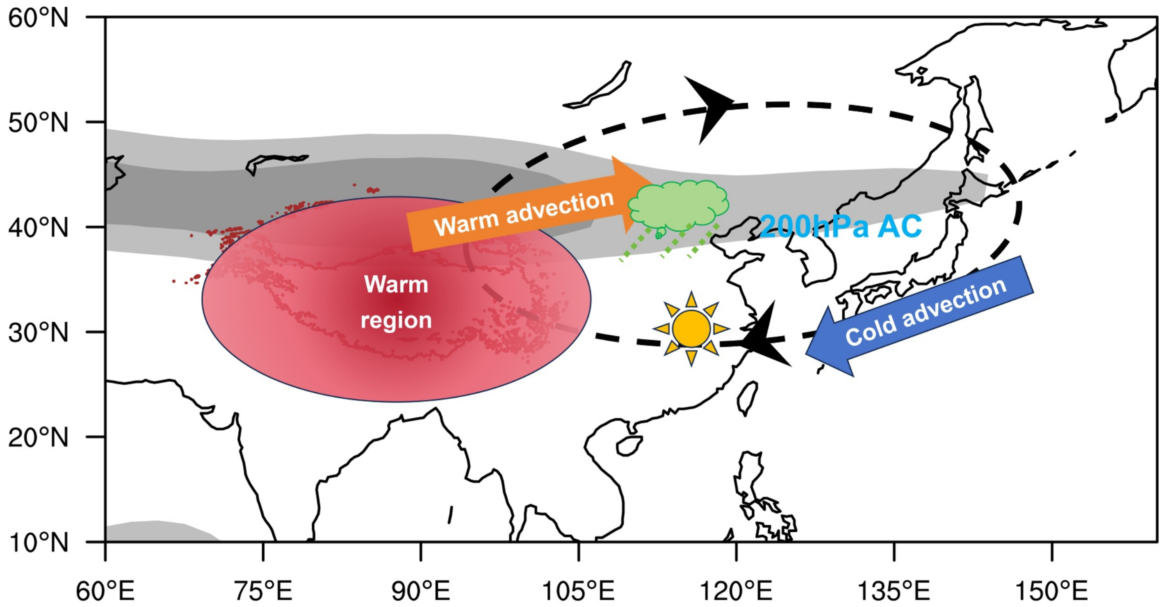

Figure 10. Schematic of the internal dynamical mode underlying the dominant mode of late-summer East Asian monsoon variability.

5. Conclusions and Discussion

This study identifies the dominant mode of interannual variability in the late-summer (July–August) East Asian summer monsoon. This mode is characterized by a troposphere-deep anomalous anticyclonic/cyclonic circulation extending across East Asia, with circulation centers exhibiting a pronounced northwestward tilt with height. It is accompanied by a tripolar pattern of precipitation anomalies, with enhanced rainfall over northern China and reduced precipitation from the Yangtze River Basin to southern Japan during the anticyclonic phase, and the opposite anomalies during the cyclonic phase. These structural features indicate that late-summer monsoon variability is fundamentally linked to large-scale upper-tropospheric circulation organization. As schematically illustrated in Figure 10, the dynamical formation of this mode and its impacts on late-summer East Asian monsoon precipitation can be summarized as follows:

- During the late-summer period, East Asian summer monsoon circulation anomalies can extract kinetic and potential energy from the subtropical background westerly jet-exit region. First, the shape of the circulation anomalies is zonally elongated, and the climatological zonal wind exhibits pronounced convergence zonally, allowing kinetic energy from the climatological flow to be converted into the kinetic energy of the anomalous circulation. Second, the anomalous circulation tilts westward with height, and the climatological temperature over East Asia exhibits a strong meridional contrast, with warmer air at lower latitudes. This configuration enables the anomalous meridional wind to transport heat from low to high latitudes, converting the available potential energy of the mean flow into that of the anomalous circulation. This result is robust across data sets with different spatial and temporal resolutions (Figure S10 in Supporting Information S1).
- Vorticity-budget diagnostics indicate that the upper-tropospheric circulation anomalies over East Asia are characterized by negative wave sources north of 40°N and positive wave sources to the south. These wave sources are primarily balanced by the MA term (Equation 12, see Methods), which represents the meridional transport of anomalous vorticity by the climatological nondivergent flow; as a result, the center of the anomalous anticyclone is dynamically anchored near 40°N. At lower atmospheric levels, negative wave sources located south of 40°N are responsible for the occurrence of an anomalous anticyclone over the area. Thus, the northwestward tilt of the late-summer anomalous anticyclone with height originates from climatological northerlies along the eastern flank of the South Asian High.
- Upper-tropospheric circulation anomalies exert a pronounced influence on anomalous vertical motion over East Asia, which in turn affects regional precipitation. Temperature advection is a key controlling factor. In northern China, significant warm advection drives anomalous upward motion, whereas from the Yangtze River Basin to southern Japan, cold advection induces anomalous subsidence. In comparison, the contribution

from vorticity advection is relatively weak. As for diabatic heating, given its complex interaction with precipitation, it is not discussed in detail here; nevertheless, it undoubtedly represents important feedback, particularly over the Yangtze River Basin and regions to its south.

Overall, our findings demonstrate that late-summer East Asian monsoon variability is dynamically sustained by jet-thermal interactions within the climatological jet-exit environment, highlighting the importance of atmospheric dynamical processes in shaping regional hydroclimate variability and associated flood-drought risks over East Asia. It is noteworthy that the late-summer East Asian summer monsoon mode identified here differs significantly from the Pacific-Japan (PJ) pattern in both its generation and maintenance. The PJ pattern is excited by tropical convective heating anomalies (R. H. Huang & Sun, 1994; Nitta, 1987), maintained primarily by baroclinic energy conversion (CP) (Kosaka & Nakamura, 2006). In contrast, our mode is situated in the East Asian jet-exit region and sustained largely by barotropic kinetic energy conversion (CK). The potential role of oceanic variability and air-sea interactions also warrant further investigation (Zhang et al., 2024).

Conflict of Interest

The authors declare no conflicts of interest relevant to this study.

Availability Statement

The data sets are available in a public repository. The data sets used in this study are publicly available. Monthly precipitation data are from the GPCP Version 2 monthly product, available at https://psl.noaa.gov/data/gridded/data.gpcp.html. The daily atmospheric reanalysis data are from the NCEP–DOE AMIP-II Reanalysis (R-2), available at https://psl.noaa.gov/data/gridded/data.ncep.reanalysis2.html. Monthly averaged ERA5 reanalysis data (Hersbach et al., 2023) used in this study are available from the Copernicus Climate Change Service Climate Data Store at https://cds.climate.copernicus.eu/datasets/reanalysis-era5-pressure-levels-monthly-means?tab=documentation. Data processing and analysis were conducted using Python (Van Rossum & Drake, 2009) and the NCAR Command Language (NCL) (2019). The analysis code supporting this study is available from the corresponding author upon reasonable request.

Acknowledgments
The work was supported by the National Key Research and Development Program of China (fund number 2024YFC3012401) and National Natural Science Foundation of China (42475046).

References

Adler, R. F., Huffman, G. J., Chang, A., Ferraro, R., Xie, P. P., Janowiak, J., et al. (2003). The version-2 global precipitation climatology project (GPCP) monthly precipitation analysis (1979–present) [Dataset]. *Journal of Hydrometeorology*, *4*(6), 1147–1167. https://doi.org/10.1175/1525-7541(2003)004<1147:TVGPCP>2.0.CO;2

Ding, Y. (1992). Summer monsoon rainfalls in China. *Journal of the Meteorological Society of Japan. Series II*, *70*(1B), 373–396. https://doi.org/10.2151/jmsj1965.70.1B_373

Ding, Y. (2004). Seasonal march of the East Asian summer monsoon. In C.-P. Chang (Ed.), *East Asian monsoon* (pp. 3–53). World Scientific. https://doi.org/10.1142/9789812701411_0001

Ding, Y., & Chan, J. C. L. (2005). The East Asian summer monsoon: An overview. *Meteorology and Atmospheric Physics*, *89*(1–4), 117–142. https://doi.org/10.1007/s00703-005-0125-z

Du, Y., Li, T., Xie, Z., & Zhu, Z. (2016). Interannual variability of the Asian subtropical westerly jet in boreal summer and its association with circulation and SST anomalies. *Climate Dynamics*, *46*(7), 2673–2688. https://doi.org/10.1007/s00382-015-2723-x

Enomoto, T., Hoskins, B. J., & Matsuda, Y. (2003). The formation mechanism of the Bonin high in August. *Quarterly Journal of the Royal Meteorological Society*, *129*(587), 157–178. https://doi.org/10.1256/qj.01.211

Feng, S., & Hu, Q. (2004). Variations in the teleconnection of ENSO and summer rainfall in northern China: A role of the Indian summer monsoon. *Journal of Climate*, *17*(24), 4871–4881. https://doi.org/10.1175/JCLI-3245.1

Han, T., Chen, H., & Wang, H. (2015). Recent changes in summer precipitation in Northeast China and the background circulation. *International Journal of Climatology*, *35*(14), 4210–4219. https://doi.org/10.1002/joc.4280

Hersbach, H., Bell, B., Berrisford, P., Biavati, G., Horányi, A., Muñoz Sabater, J., et al. (2023). ERA5 monthly averaged data on pressure levels from 1940 to present [Dataset]. *Copernicus Climate Change Service (C3S) Climate Data Store (CDS)*. https://doi.org/10.24381/cds.6860a573

Holton, J. R., & Hakim, G. J. (2013). *An introduction to dynamic meteorology* (5th ed.). Academic Press.

Hu, K., Huang, G., Wu, R., & Wang, L. (2018). Structure and dynamics of a wave train along the wintertime Asian jet and its impact on East Asian climate. *Climate Dynamics*, *51*(11), 4123–4137. https://doi.org/10.1007/s00382-017-3674-1

Huang, G., & Liu, Y. (2011). Simulation of the East Asian subtropical westerly jet stream with GFDL AGCM (AM2.1). *Atmospheric and Oceanic Science Letters*, *4*(1), 24–29. https://doi.org/10.1080/16742834.2011.11446902

Huang, R. H., & Sun, F. Y. (1994). Impacts of the thermal state and the convective activities in the tropical western warm pool on the summer climate anomalies in East Asia. *Chinese Journal of Atmospheric Sciences*, *18*(2), 141–151. https://doi.org/10.3878/j.issn.1006-9895.1994.02.02

Kanamitsu, M., Ebisuzaki, W., Woollen, J., Yang, S.-K., Hnilo, J. J., Fiorino, M., & Potter, G. L. (2002). NCEP–DOE AMIP-II reanalysis (R-2) [Dataset]. *Bulletin of the American Meteorological Society*, *83*(11), 1631–1644. https://doi.org/10.1175/BAMS-83-11-1631

Kosaka, Y., & Nakamura, H. (2006). Structure and dynamics of the summertime Pacific–Japan teleconnection pattern. *Quarterly Journal of the Royal Meteorological Society*, *132*(619), 2009–2030. https://doi.org/10.1256/qj.05.204

Kosaka, Y., Nakamura, H., Watanabe, M., & Kimoto, M. (2009). Analysis on the dynamics of a wave-like teleconnection pattern along the summertime Asian jet based on a reanalysis dataset and climate model simulations. *Journal of the Meteorological Society of Japan. Ser. II*, *87*(3), 561–580. https://doi.org/10.2151/jmsj.87.561

Lau, K. M. (1992). East Asian summer monsoon rainfall variability and climate teleconnection. *Journal of the Meteorological Society of Japan. Series II*, *70*(1B), 211–242. https://doi.org/10.2151/jmsj1965.70.1B_211

Li, S., Kucharski, F., Yang, J., Gong, Z., Zhao, Y., & Feng, G. (2024). The interdecadal changes of the relationship between May–June and July–August NWPSH and their physical mechanisms. *Geophysical Research Letters*, *51*(19), e2024GL111289. https://doi.org/10.1029/2024GL111289

Li, T., & Gao, S. (1995). Synoptic situation of the 94.7 torrential rain in Beijing. *Meteorological Monthly*, *21*(10), 24–26.

Li, X., Li, W., Zhou, X., Hong, H., Gao, H., & Sun, L. (2025). Analysis of the rainfall background and implications of the "25–7" regional major flood in the Haihe River Basin. *China Flood & Drought Management*, *35*(11). 1–5, 11. https://doi.org/10.16867/j.issn.1673-9264.2025510

Lu, R. (2004). Associations among the components of the East Asian summer monsoon system in the meridional direction. *Journal of the Meteorological Society of Japan. Series II*, *82*(1), 155–165. https://doi.org/10.2151/jmsj.82.155

Lu, R. Y., Oh, J. H., & Kim, B. J. (2002). A teleconnection pattern in upper-level meridional wind over the North African and Eurasian continent in summer. *Tellus A: Dynamic Meteorology and Oceanography*, *54*(1), 44–55. https://doi.org/10.3402/tellusa.v54i1.12122

Lu, T., Hu, K., Huang, G., & Wang, Y. (2024). Optimal atmospheric heat sources for the interannual variability of South Asian summer monsoon. *Geophysical Research Letters*, *51*(21), e2024GL112059. https://doi.org/10.1029/2024GL112059

Lu, T., Hu, K., Huang, G., Yeh, S. W., & Wang, Y. (2025). Energetic processes underlying the interannual variability of the South Asian summer monsoon. *npj Climate and Atmospheric Sciences*, *8*(1), 300. https://doi.org/10.1038/s41612-025-01143-4

Ma, M., Qu, Y., Lyu, J., Zhang, X., Su, Z., Gao, H., et al. (2022). The 2022 extreme drought in the Yangtze River Basin: Characteristics, causes and response strategies. *River*, *1*(2), 162–171. https://doi.org/10.1002/rvr2.23

NCAR Command Language (NCL). (2019). [Software]. *UCAR/NCAR/CISL/TDD*. Retrieved from https://www.ncl.ucar.edu

Nitta, T. (1987). Convective activities in the tropical western Pacific and their impact on the Northern Hemisphere summer circulation. *Journal of the Meteorological Society of Japan. Ser. II*, *65*(3), 373–390. https://doi.org/10.2151/jmsj1965.65.3_373

North, G. R., Bell, T. L., Cahalan, R. F., & Moeng, F. J. (1982). Sampling errors in the estimation of empirical orthogonal functions. *Monthly Weather Review*, *110*(7), 699–706. https://doi.org/10.1175/1520-0493(1982)110<0699:SEITEO>2.0.CO;2

Sardeshmukh, P. D., & Hoskins, B. J. (1988). The generation of global rotational flow by steady idealized tropical divergence. *Journal of the Atmospheric Sciences*, *45*(7), 1228–1251. https://doi.org/10.1175/1520-0469(1988)045<1228:TGOGRF>2.0.CO;2

Seo, K. H., Son, J. H., Lee, S. E., Tomita, T., & Park, H. S. (2012). Mechanisms of an extraordinary East Asian summer monsoon event in July 2011. *Geophysical Research Letters*, *39*(5), L06703. https://doi.org/10.1029/2011GL050378

Simmons, A. J., Wallace, J. M., & Branstator, G. W. (1983). Barotropic wave propagation and instability, and atmospheric teleconnection patterns. *Journal of the Atmospheric Sciences*, *40*(6), 1363–1392. https://doi.org/10.1175/1520-0469(1983)040<1363:BWPAIA>2.0.CO;2

Trenberth, K. E. (1978). On the interpretation of the diagnostic quasi-geostrophic omega equation. *Monthly Weather Review*, *106*(1), 131–137. https://doi.org/10.1175/1520-0493(1978)106<0131:OTIOTD>2.0.CO;2

Van Rossum, G., & Drake, F. L. (2009). Python 3 Reference Manual [Software]. *Python Software Foundation*. https://www.python.org

Wang, B. (1992). The vertical structure and development of the ENSO anomaly mode during 1979–1989. *Journal of the Atmospheric Sciences*, *49*(8), 698–712. https://doi.org/10.1175/1520-0469(1992)049<0698:TVSADO>2.0.CO;2

Wang, B., Liu, J., Yang, J., Zhou, T., & Wu, Z. (2009). Distinct principal modes of early and late summer rainfall anomalies in East Asia. *Journal of Climate*, *22*(13), 3864–3875. https://doi.org/10.1175/2009JCLI2850.1

Wang, B., Wu, R., & Lau, K. M. (2001). Interannual variability of the Asian summer monsoon: Contrasts between the Indian and the western North Pacific–East Asian monsoons. *Journal of Climate*, *14*(20), 4073–4090. https://doi.org/10.1175/1520-0442(2001)014<4073:IVOTAS>2.0.CO;2

Wang, B., Zhang, M., Wei, J., Wang, S., Li, X., Li, S., et al. (2013). Changes in extreme precipitation over Northeast China, 1960–2011. *Quaternary International*, *298*, 177–186. https://doi.org/10.1016/j.quaint.2013.01.025

Watanabe, M. (2005). *Linear Baroclinic Model (LBM) Package Users' Guide*. Center for Climate System Research, University of Tokyo. Retrieved from https://ccsr.aori.u-tokyo.ac.jp/~lbm/lbm/doc2.2.pdf

Wei, W., Zhang, R., Wen, M., & Yang, S. (2017). Relationship between the Asian westerly jet stream and summer rainfall over Central Asia and North China: Roles of the Indian monsoon and the South Asian high. *Journal of Climate*, *30*(2), 537–552. https://doi.org/10.1175/JCLI-D-15-0814.1

Yanai, M., Esbensen, S., & Chu, J.-H. (1973). Determination of bulk properties of tropical cloud clusters from large-scale heat and moisture budgets. *Journal of the Atmospheric Sciences*, *30*(4), 611–627. https://doi.org/10.1175/1520-0469(1973)030<0611:DOBPOT>2.0.CO;2

Yin, Z., Yang, S., & Wei, W. (2023). Quantitative attribution of vertical motions responsible for the early spring drought conditions over southeastern China. *Climate Dynamics*, *61*(5), 2655–2672. https://doi.org/10.1007/s00382-023-06708-8

Yu, X. (2012). Investigation of the Beijing extreme flooding event on 21 July 2012. *Meteorological Monthly*, *38*(11), 1313–1329. https://doi.org/10.7519/j.issn.1000-0526.2012.11.001

Zhang, D., Song, J., Gao, Y., Peng, Y., Hu, J., Schmitt, F. G., & Huang, Y. (2024). Scale-to-scale energy flux in the oceanic global circulation models. *Frontiers in Marine Science*, *11*, 1307751. https://doi.org/10.3389/fmars.2024.1307751